SCISPACE
formerly Typeset

Open access • Journal Article • DOI:10.1097/RLI.0000000000000171

Advanced virtual monoenergetic computed tomography of hyperattenuating and hypoattenuating liver lesions: ex-vivo and patient experience in various body sizes

— Source link

Daniela B. Husarik, Sonja Gordic, Lotus Desbiolles, Bernhard Krauss ...+6 more authors

Institutions: University of Zurich, Kantonsspital St. Gallen, Siemens

Published on: 01 Oct 2015 - Investigative Radiology (Invest Radiol)

Related papers:

- Assessment of an advanced image-based technique to calculate virtual monoenergetic computed tomographic images from a dual-energy examination to improve contrast-to-noise ratio in examinations using iodinated contrast media.
- Dual-energy MDCT in hypervascular liver tumors: effect of body size on selection of the optimal monochromatic energy level.
- Maximizing Iodine Contrast-to-Noise Ratios in Abdominal CT Imaging through Use of Energy Domain Noise Reduction and Virtual Monoenergetic Dual-Energy CT
- Dual- and Multi-Energy CT: Principles, Technical Approaches, and Clinical Applications
- Assessment of an Advanced Monoenergetic Reconstruction Technique in Dual-Energy Computed Tomography of Head and Neck Cancer.

Share this paper:

View more about this paper here: https://typeset.io/papers/advanced-virtual-monoenergetic-computed-tomography-of-2j9zs19if3

University of Zurich[UZH]

Zurich Open Repository and Archive
University of Zurich
University Library
Strickhofstrasse 39
CH-8057 Zurich
www.zora.uzh.ch

Year: 2015

Advanced virtual monoenergetic computed tomography of hyperattenuating and hypoattenuating liver lesions: ex-vivo and patient experience in various body sizes

Husarik, Daniela B ; Gordic, Sonja ; Desbiolles, Lotus ; Krauss, Bernhard ; Leschka, Sebastian ; Wildermuth, Simon ; Alkadhi, Hatem

Abstract: OBJECTIVE: To determine the value of advanced virtual monoenergetic images (mono+) from dual-energy computed tomography (CT) of hyperattenuating and hypoattenuating liver lesions in various phantom sizes and patients in comparison with standard monoenergetic images (mono). MATERIALS AND METHODS: Anthropomorphic phantoms simulating 4 patient sizes (S, 300 × 200 mm; M, 350 × 250 mm; L, 400 × 300 mm; and XL, 600 × 450 mm) with a liver insert containing both hyperattenuating and hypoattenuating iodine-containing lesions were imaged with dose-equivalent dual-energy (100/150 Sn kilovolt [peak] [kVp]) and single-energy (120 kV[p]) protocols on a 192-slice dual-source CT system. In addition, 4 patients with 3 hypoattenuating and 3 hyperattenuating hepatocellular carcinoma were included and underwent dual-energy CT imaging with the same scanner at similar kV(p) settings (100/150 Sn kV[p]). Images were reconstructed with standard mono and with the mono+ algorithm at 10-kiloelectron volt (keV) intervals from 40 to 190 keV. Attenuation of the liver and lesions were measured, and contrast-to-noise ratios (CNRs) were calculated. Lesion conspicuity was rated by 2 blinded independent readers in all mono and mono+ data sets from 40 to 190 keV using a 5-point Likert scale (1, lowest conspicuity; and 5, highest conspicuity). RESULTS: Attenuation in the liver and in both hyperattenuating and hypoattenuating lesions did not differ between mono and mono+ ($P = 0.41$-0.49). Noise on mono+ was significantly lower than on mono for all phantom sizes ($P < 0.05$) and was increasing with phantom size. Hyperattenuating lesion CNR was highest for mono+ images at 40 keV in the S phantom (6.73), with significantly higher CNR for mono+ than for mono and for single energy (120 kV[p]) in all phantom sizes (all $P < 0.001$) except for the XL phantom. Hypoattenuating lesion CNR was highest for high-keV mono+ being significantly higher than on mono and on single-energy (120 kV[p]) images (all $P < 0.001$), except for the XL phantom with significantly higher CNR for mono (1.3) compared with mono+ (0.47) and 120 kV(p) (1.26). In patients, CNR curves of hyperattenuating hepatocellular carcinoma were in accordance with the phantom data, whereas hypoattenuating lesions demonstrate varying curves, some being in accordance with findings in phantoms. Interreader agreement for lesion conspicuity was very good (intraclass correlation, 0.95), with higher conspicuity scores for mono+ than for mono and single energy (120 kV[p]) at all phantom sizes (all $P < 0.05$) and within patients. CONCLUSION: Our ex vivo and patient data demonstrate added value for imaging of both hyperattenuating and hypoattenuating liver lesions with advanced virtual monoenergetic dual-energy CT by decreased noise, increased CNR, and higher lesion conspicuity, although with limitations in XL body sizes.

DOI: https://doi.org/10.1097/RLI.0000000000000171

Posted at the Zurich Open Repository and Archive, University of Zurich
ZORA URL: https://doi.org/10.5167/uzh-111468

Journal Article
Published Version

Originally published at:
Husarik, Daniela B; Gordic, Sonja; Desbiolles, Lotus; Krauss, Bernhard; Leschka, Sebastian; Wildermuth, Simon; Alkadhi, Hatem (2015). Advanced virtual monoenergetic computed tomography of hyperattenuating and hypoattenuating liver lesions: ex-vivo and patient experience in various body sizes. Investigative Radiology, 50(10):695-702.
DOI: https://doi.org/10.1097/RLI.0000000000000171

Advanced Virtual Monoenergetic Computed Tomography of Hyperattenuating and Hypoattenuating Liver Lesions

Ex-Vivo and Patient Experience in Various Body Sizes

Daniela B. Husarik, MD, Sonja Gordic, MD,* Lotus Desbiolles, MD,*† Bernhard Krauss, PhD,‡ Sebastian Leschka, MD,*† Simon Wildermuth, MD,† and Hatem Alkadhi, MD, MPH, EBCR**

Objective: To determine the value of advanced virtual monoenergetic images (mono+) from dual-energy computed tomography (CT) of hyperattenuating and hypoattenuating liver lesions in various phantom sizes and patients in comparison with standard monoenergetic images (mono).

Materials and Methods: Anthropomorphic phantoms simulating 4 patient sizes (S, 300 × 200 mm; M, 350 × 250 mm; L, 400 × 300 mm; and XL, 600 × 450 mm) with a liver insert containing both hyperattenuating and hypoattenuating iodine-containing lesions were imaged with dose-equivalent dual-energy (100/150 Sn kilovolt [peak] [kV{p}]) and single-energy (120 kV[p]) protocols on a 192-slice dual-source CT system. In addition, 4 patients with 3 hypoattenuating and 3 hyperattenuating hepatocellular carcinoma were included and underwent dual-energy CT imaging with the same scanner at similar kV (p) settings (100/150 Sn kV[p]). Images were reconstructed with standard mono and with the mono+ algorithm at 10–kiloelectron volt (keV) intervals from 40 to 190 keV. Attenuation of the liver and lesions were measured, and contrast-to-noise ratios (CNRs) were calculated. Lesion conspicuity was rated by 2 blinded independent readers in all mono and mono+ data sets from 40 to 190 keV using a 5-point Likert scale (1, lowest conspicuity; and 5, highest conspicuity).

Results: Attenuation in the liver and in both hyperattenuating and hypoattenuating lesions did not differ between mono and mono+ (P = 0.41–0.49). Noise on mono+ was significantly lower than on mono for all phantom sizes (P < 0.05) and was increasing with phantom size. Hyperattenuating lesion CNR was highest for mono+ images at 40 keV in the S phantom (6.73), with significantly higher CNR for mono+ than for mono and for single energy (120 kV[p]) in all phantom sizes (all P < 0.001) except for the XL phantom. Hypoattenuating lesion CNR was highest for high-keV mono+ being significantly higher than on mono and on single-energy (120 kV[p]) images (all P < 0.001), except for the XL phantom with significantly higher CNR for mono (1.3) compared with mono+ (0.47) and 120 kV(p) (1.26). In patients, CNR curves of hyperattenuating hepatocellular carcinoma were in accordance with the phantom data, whereas hypoattenuating lesions demonstrate varying curves, some being in accordance with findings in phantoms. Interreader agreement for lesion conspicuity was very good (intraclass correlation, 0.95), with higher conspicuity scores for mono+ than for mono and single energy (120 kV[p]) at all phantom sizes (all P < 0.05) and within patients.

Conclusion: Our ex vivo and patient data demonstrate added value for imaging of both hyperattenuating and hypoattenuating liver lesions with advanced virtual monoenergetic dual-energy CT by decreased noise, increased CNR, and higher lesion conspicuity, although with limitations in XL body sizes.

Key Words: dual energy, CT, monoenergetic, liver, low contrast conspicuity

(*Invest Radiol* 2015;00: 00–00)

Reduction of radiation dose in computed tomography (CT) has been successfully implemented in various body regions and indications, primarily by tube voltage lowering[1] and by making use of the improved image quality with iterative reconstruction algorithms.[2,3] However, there still exist controversies about the lowest possible radiation dose level avoiding loss of diagnostic information.[4,5]

Dual-energy CT acquires data at 2 tube voltage levels, which allow for monoenergetic extrapolations, resulting in virtual monoenergetic images (hereafter called *mono*) at a wide range of photon energies.[6] Because of the energy-dependent photoelectric effect, information about an element can be obtained from the attenuation at different photon energies, which enable the differentiation of material composition. This advantage has been used in previous studies to reduce metal artifacts.[7] Another application of mono is related to the improvement of iodine contrast in low–kiloelectron volt images, which was shown advantageous in CT angiography.[8–10] In a recent study, Sudarski et al[11] demonstrated that monoenergetic images at 70 keV compared to polyenergetic images at 120 kilovolt (peak) (kV[p]) improve the image quality and diagnostic confidence for assessing liver metastases of gastrointestinal stromal tumors. However, in this study, authors noted that the contrast-to-noise ratio (CNR) of lesions on low-keV mono images was significantly lower compared to standard 120-kV(p) images owing to high image noise.[11]

Recently, an advanced monoenergetic image reconstruction algorithm (hereafter called *mono+*) has been introduced, which is characterized by a combination of the high-contrast properties of low-keV images and the low image noise of high-keV images.[12] First preliminary results indicated a benefit of using this mono+ algorithm for hyperattenuating liver lesions compared to standard mono images.[12] This algorithm, however, might be also advantageous for improving the low contrast conspicuity of liver CT, as standard mono images might suffer from high noise.[11] To the best of our knowledge, no study has evaluated the mono+ algorithm in both hyperattenuating and hypoattenuating liver lesions, and none investigated into the influence of various body sizes. In addition, no data in patients with liver lesions have been reported so far.

Thus, the purpose of this study was to determine the value of the advanced mono+ algorithm in image quality, noise, CNR, and lesion conspicuity of hyperattenuating and hypoattenuating liver lesions in various phantom sizes and in patients with hepatocellular carcinoma (HCC) in comparison with standard mono images from dual-energy CT.

MATERIALS AND METHODS

Phantom

For the phantom part of the study, a custom-built anthropomorphic abdominal phantom (QSA-453, QRM, Moehrendorf, Germany) was used including extension rings to simulate 4 patient sizes (S,

Received for publication February 6, 2015; and accepted for publication, after revision, April 8, 2015.

From the *Institute of Diagnostic and Interventional Radiology, University Hospital Zurich, Zurich; †Division of Radiology and Nuclear Medicine, Kantonsspital St. Gallen, St. Gallen, Switzerland; and ‡Siemens, Siemens Healthcare, Forchheim, Germany.

Conflicts of interest and sources of funding: Bernhard Krauss in an employee of Siemens Healthcare. For the remaining authors, none were declared. Authors without pertinent disclosures maintained full control of the data and information submitted.

Reprints: Hatem Alkadhi, MD, MPH, EBCR, Institute of Diagnostic and Interventional Radiology, University Hospital Zurich, Raemistrasse 100, CH-8091 Zurich, Switzerland. E-mail: hatem.alkadhi@usz.ch.

Copyright © 2015 Wolters Kluwer Health, Inc. All rights reserved.

ISSN: 0020-9996/15/0000–0000

Copyright © 2015 Wolters Kluwer Health, Inc. Unauthorized reproduction of this article is prohibited.

300 × 200 mm; M, 350 × 250 mm; L, 400 × 300 mm; and XL, 600 × 450 mm). The central portion of the phantom contained a liver insert (90 Hounsfield units [HU] at 120 kV[p], not containing iodine) with spherical and capsular hyperattenuating and hypoattenuating iodine-containing lesions (5–15 mm, 45 HU, 60 HU, 120 HU, and 180 HU at 120 kV[p]) composed of a homogeneous resin (Fig. 1). The hyperattenuating and hypoattenuating lesions were composed to simulate lesions in the late arterial phase at different CT tube voltage settings. Thirty lesions were scattered throughout the liver insert in a perceived random fashion. The construction map was used as a standard of reference for lesion position.

Patients

In addition to the ex vivo experiments, 4 patients with a total of 3 hyperattenuating and 3 hypoattenuating HCCs (median age, 58 years; 3 men and 1 woman) were included in this study. The size of the hyperattenuating lesions were as follows: mean, 22 × 17.3 mm; median, 18 × 17 mm; range, 18–30 × 12–23 mm; the sizes of the hypoattenuating lesions were the following: mean, 19.7 × 17.7 mm; median, 14 × 12 mm; range, 12–33 × 9–32 mm.

CT Image Acquisition and Reconstruction

Imaging was performed on a third-generation 2 × 192-slice dual-source CT (SOMATOM Force, Siemens Healthcare Sector, Forchheim, Germany) with an integrated high-resolution circuit Stellar detector (Stellar Technology; Siemens).[13] The phantoms were imaged with a tube voltage of 100 kV(p) for tube A (reference tube current-time product, 240 milliampere second [mA s]) and 150 Sn kV(p) with a tin filter for tube B (reference tube current-time product, 120 mA s) using automatic attenuation-based tube current modulation (CareDose, Siemens). For detailed imaging parameters, see Table 1. In addition, phantoms were scanned with dose-equivalent single-energy CT at 120 kV(p).

Patients were imaged according to our institutional standard dual-energy protocol of the abdomen with a tube voltage pair of 100/150 Sn and a reference tube current-time product of 345/175 mA s after injection of 70-mL Iopromide (Ultravist 300) at 5 mL/s followed by a 20-mL saline flush injected at 5 mL/s. Imaging was initiated with a 9-second delay after a threshold of 100 HU was reached in the aorta. All CT examinations in patients were clinically indicated.

All images in phantoms and patients were reconstructed with a slice thickness of 1.5 mm, an increment of 1 mm, a field-of-view of 450 mm, and an image matrix of 512 × 512 pixels. Using a standard postprocessing software (*syngo*.via VA40, Siemens), mono and mono + images were calculated at photon energies ranging from 40 to 190 keV at 10-keV intervals.

Radiation Dose Estimation

For radiation dose estimations, the CT volume dose index (in mGy) and the dose length product (DLP, in mGy cm) were derived from the electronically logged protocols.

Quantitative Data Analysis

Attenuation of the liver and one hyperattenuating (15 × 22.5 mm, 180 HU at 120 kV[p]), and one hypoattenuating oval lesion (15 × 22.5 mm, 45 HU at 120 kV[p]) were measured on all data sets

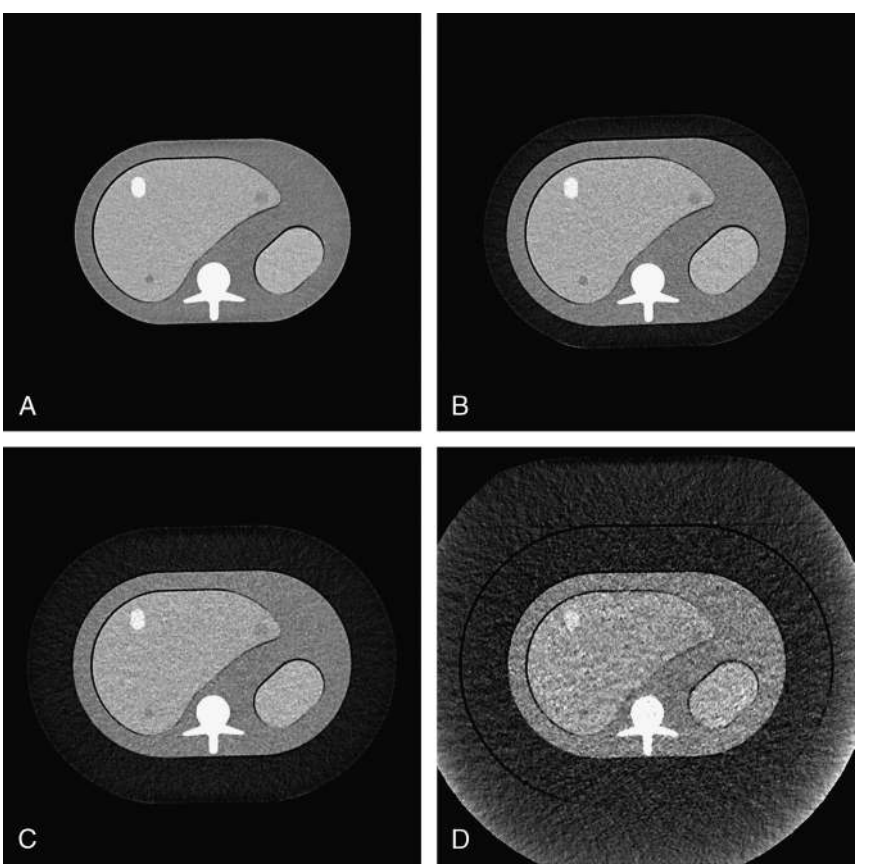

FIGURE 1. Representative axial CT images of the small (A), medium (B), large (C), and extralarge (D) phantoms containing one hyperattenuating and 2 hypoattenuating lesions.

© 2015 Wolters Kluwer Health, Inc. All rights reserved.

Copyright © 2015 Wolters Kluwer Health, Inc. Unauthorized reproduction of this article is prohibited.

TABLE 1. Dual-energy CT Scanning Parameters

	Dual Energy			Single Energy 120 kV(p)	
	mA s eff / mA s ref Tube A 100 kV(p)	mA s eff / mA s ref Tube B Sn 150 kV(p)	$CTDI_{vol}$	mA s/ref	$CTDI_{vol}$
S	90/240	52/120	5.45	77/118	5.17
M	141/240	74/120	8.32	117/112	7.85
L	214/240	106/120	12.41	182/195	12.26
XL	521/240	210/120	28.74	432/204	29.02

$CTDI_{vol}$ indicates CT volume dose index; mA s eff, effective mA s; mA s ref, reference tube mA s.

(mono and mono+ at 10-keV intervals between 40 and 190 keV and single energy at 120 kV[p]) using a circular region-of-interest (ROI) with an average size of 87.4 mm^2.

In vivo CNR analysis was performed of 3 hyperattenuation and 3 hypoattenuation lesions (mean ROI size, 87.3 ROI mm^2).

Contrast-to-noise ratios were calculated for the hyperattenuating and the hypoattenuating lesions in the phantom and patients using the following formula: $CNR = \left|(ROI\ Liver - ROI\ Lesion) / Noise\right|$. For noise, the standard deviation (SD) of HU in a ROI placed in the background tissue (phantom) or muscle (patients) was used.

Qualitative Data Analysis

Rating of lesion conspicuity was performed by 2 blinded and independent readers on mono and mono+ images at 10-keV intervals between 40 and 190 keV and on single-energy (120 kV[p]) images using a 5-point Likert scale (based on European guidelines on Quality criteria

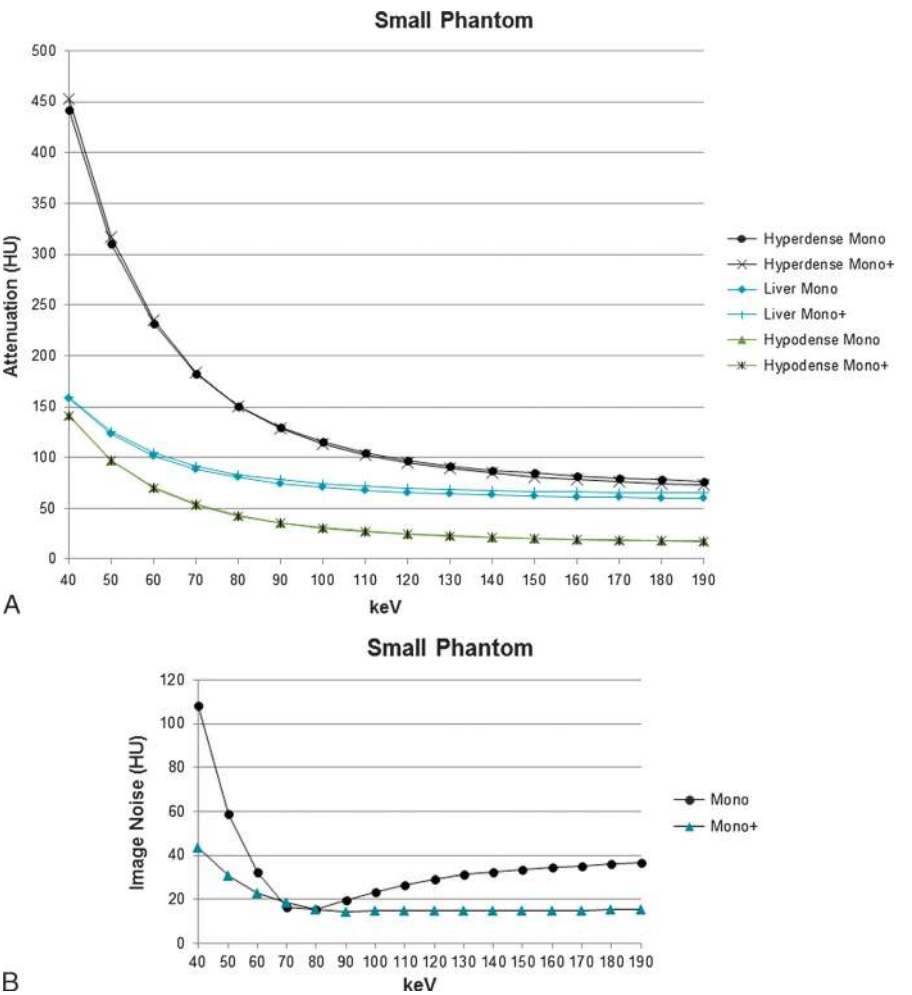

FIGURE 2. A, Attenuation values in the small phantom of the liver, the hypoattenuating and the hyperattenuating lesions on monoenergetic (mono) and advanced monoenergetic (mono+) images. B, Image noise in the small phantom on mono and mono+, being lower for mono+ compared to mono images particularly at low energy levels.

© 2015 Wolters Kluwer Health, Inc. All rights reserved.

Copyright © 2015 Wolters Kluwer Health, Inc. Unauthorized reproduction of this article is prohibited.

for CT[14]): 1, lowest conspicuity; cannot identify or rule out lesion; 2, low conspicuity; lesion will be potentially missed; 3, medium conspicuity; will probably not miss lesion; 4, high conspicuity; most likely will identify lesion; 5, highest conspicuity; lesion can be detected without diagnostic compromise.

A total of 4 lesions were evaluated including 2 hyperattenuating (180 HU, 10 mm; and 120 HU, 5 mm) and 2 hypoattenuating lesions (60 HU, 10 mm; and 45 HU, 5 mm).

Statistical Analysis

Statistical analysis was performed using commercially available software (SPSS release 22 for Windows, SPSS Inc, Chicago, IL). Descriptive values are given as numbers and frequencies, and numerical values are given as mean. Continuous data (attenuation, noise, CNR) were compared using a paired *t* test. Interreader agreement on lesion conspicuity in the phantom was assessed by calculating intraclass correlation. Agreement between readers was interpreted according to Landis and Koch as poor, less than 0.20; fair, 0.21 to 0.40; moderate, 0.41 to 0.60; good, 0.61 to 0.80; and very good, 0.81 to 1.00.[15] A 2-sided $P < 0.05$ was considered to indicate statistical significance.

RESULTS

Radiation Dose Estimation

The CT volume dose index increased with increasing phantom size for both-dual energy (S, 5.45 mGy; M, 8.32 mGy; L, 12.41 mGy;

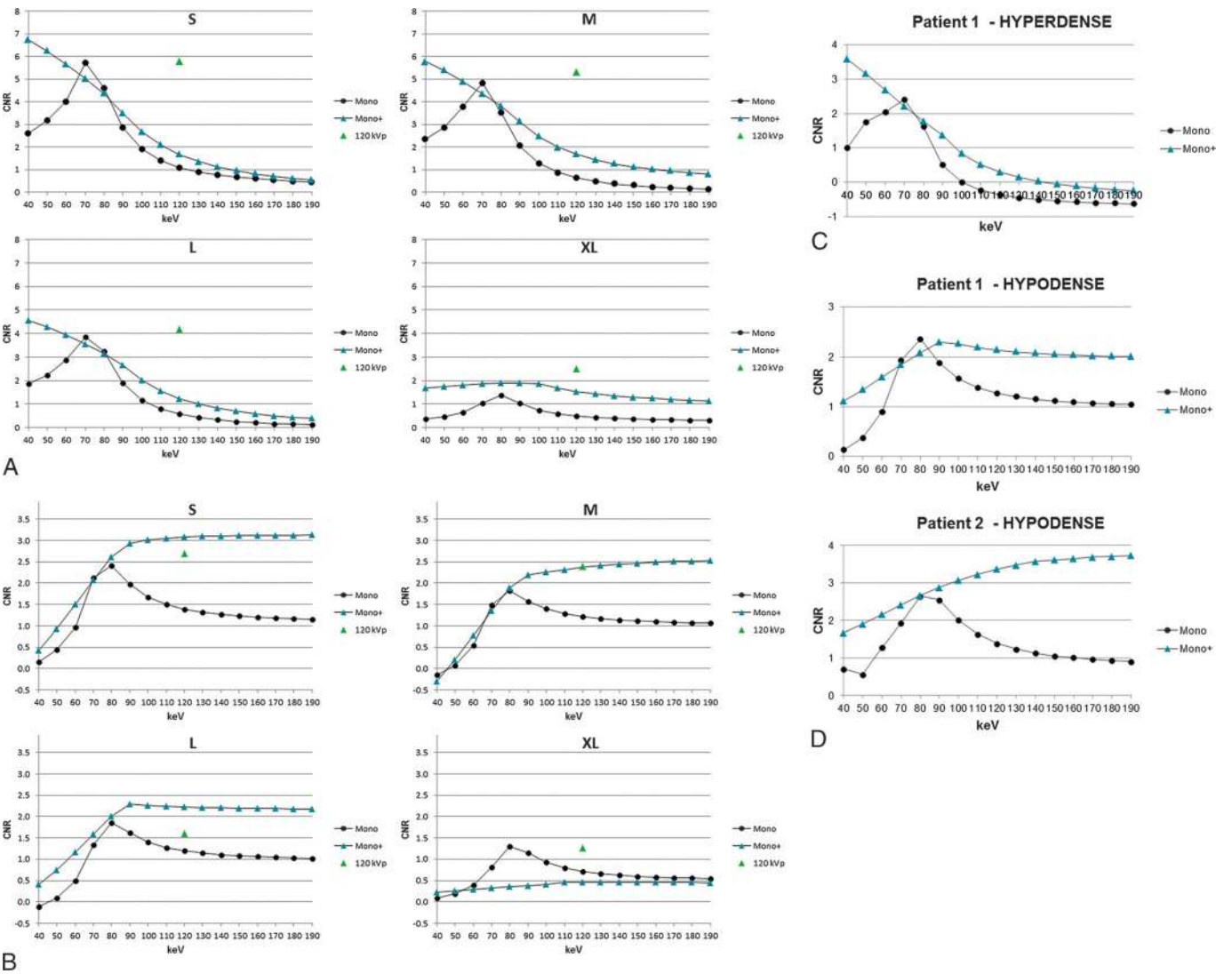

FIGURE 3. A, Contrast-to-noise ratio (CNR) of hyperattenuating liver lesions in all phantom sizes on mono, mono+, and on single-energy 120-kV (p) images. Note the highest values in all phantoms on mono+ images, an effect that is pronounced at low energy levels, except in the XL phantom, where the highest values were found on single-energy 120-kV(p) images. B, Contrast-to-noise ratio of hypoattenuating liver lesion in all phantom sizes on mono, mono+, and on single-energy 120-kV(p) images. Note the highest values in the small, medium, and large phantoms on mono+ images, whereas for the XL phantom, highest CNR was found on mono and single-energy 120-kV(p) images. C, Contrast-to-noise ratio of a hyperattenuating liver lesion in a patient with HCC on mono and mono+ images. Note the high values in low–kiloelectron volt mono+, and the CNR peak at 70 keV on mono images. D, Contrast-to-noise ratio of the hypoattenuating liver lesion in 2 patients on mono and mono+ images. Note the increasing CNR with increasing kiloelectron volt on mono+ images with a small or no peak and CNR peak at 70 to 90 keV on mono images.

© 2015 Wolters Kluwer Health, Inc. All rights reserved.

Copyright © 2015 Wolters Kluwer Health, Inc. Unauthorized reproduction of this article is prohibited.

and XL, 28.74 mGy) and single-energy protocols (S, 5.17 mGy; M, 7.85 mGy; L, 12.26 mGy; and XL, 29.02 mGy).

Quantitative Data Analysis

Attenuation of the liver and lesions (both hyperattenuating and hypoattenuating) did not differ between mono and mono+ images (P = 0.41-0.49). In all phantom sizes, attenuation decreased with increasing kiloelectron volt (Fig. 2A).

Image noise on mono+ was significantly lower than on mono for all phantom sizes (all $P < 0.05$) with highest noise on 40 keV images (ranging from 109 HU (S-mono) and 44 HU (S-mono+) to 388 HU (mono XL) and 150 HU (XL-mono+). With lower kiloelectron volt, image noise decreased on both mono and mono+ (Fig. 2B). Image noise was lowest on 80-keV images for mono in all phantom sizes (S, 15 HU; M, 20 HU; L, 20 HU; and XL, 39 HU) and was significantly lower on mono+ in all phantom sizes (S, 14 HU at 90 keV; M, 18 HU at 90 keV; L, 18 HU at 90 keV; and XL, 36 HU at 110 keV); all $P < 0.05$. On single-energy images, noise did not differ significantly from mono+ (S, 14 HU; M, 15 HU; L, 16 HU; and XL, 37 HU; $P = 0.11$).

The CNR of hyperattenuating liver lesions was highest for mono + at 40 keV in the S phantom (6.73), with significantly higher CNR on mono+ than on mono in all phantom sizes (S, 6.73 vs. 5.7; M, 5.8 vs. 4.8; L, 4.5 vs. 3.8; XL, 1.9 vs. 1.4; all $P < 0.001$) and higher CNR on mono + than on single energy (120 kV[p]) in all but the XL phantom (S: 5.8, M: 5.3, L: 4.2, XL: 2.5) (Fig. 3A).

The CNR of hypoattenuating liver lesions was highest for high keV mono+ (160-190 keV) (3.12 in the S phantom). The CNR on mono+ was significantly higher than on mono (S, 3.1 vs. 2.4; M, 2.5 vs. 1.8; L, 2.3 vs. 1.9; all $P < 0.001$) and single energy (S, 2.7; M, 2.4; and L, 1.6) except for the XL phantom with significantly higher CNR for the mono (1.3) and single energy (120 kV[p]; 1.3) compared to the mono+ images (0.5) (Fig. 3B).

In patients, CNR of hyperattenuating HCC demonstrated similar curves with high values on low–kiloelectron volt mono+ images and a CNR peak at 70 keV on mono images (Fig. 3C). In patients, hypoattenuating lesions demonstrated varying CNR curves, some in accordance with the phantom results, with increasing CNR on higher-kiloelectron volt images on mono+ images. One patient showed continuous increase in CNR with keV on mono+ images, the other 2 patients a low peak at 90 keV. The CNR on mono images in all 3 patients showed a peak between 70 and 90 keV (Fig. 3D). The CNR on high–kiloelectron volt mono+ images is higher than on low–kiloelectron volt images. Representative examples are provided in Figure 4.

Qualitative Data Analysis

Interreader agreement for lesion conspicuity was very good (intraclass correlation, 0.95). Lesion conspicuity scores were significantly higher for mono+ than for mono and single-energy images (all $P < 0.05$) for both readers and for both hyperattenuating and hypoattenuating liver lesions (Fig. 5), except in the XL phantom, where none of the hypoattenuating lesions could be detected at any kiloelectron volt setting. Overall, conspicuity scores decreased with increasing phantom size (Table 2). Hyperattenuating lesions were more conspicuous on low– kiloelectron volt images and hypoattenuating lesions on high–kiloelectron volt images, with better scores for mono+

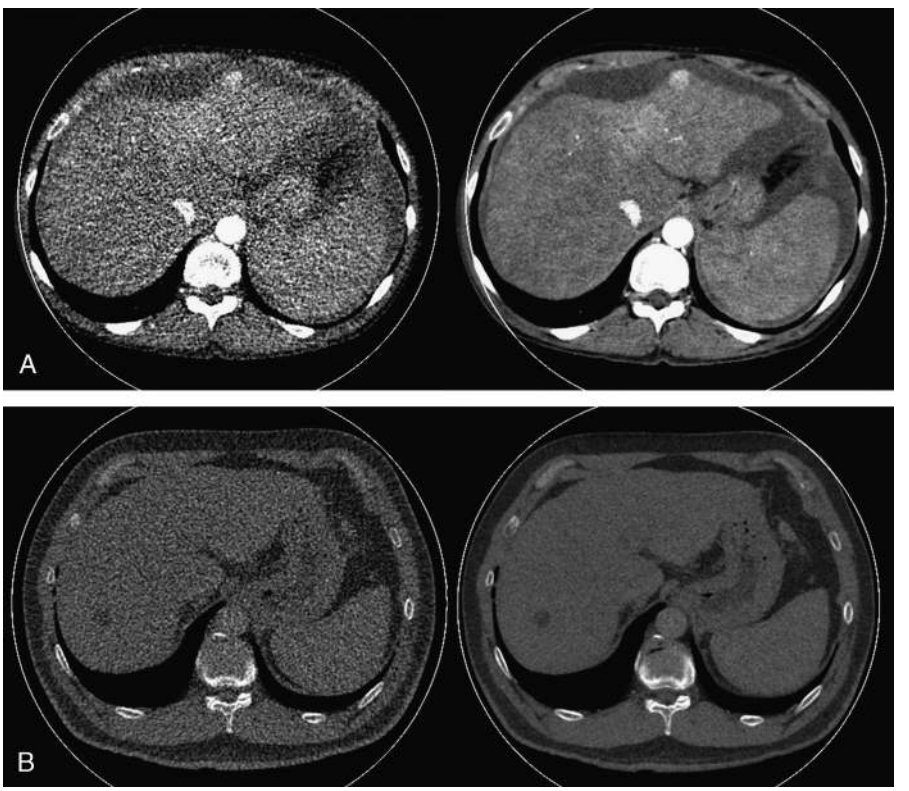

FIGURE 4. A, Axial images at 40 keV with mono (left) and mono + (right) of a 47-year-old patient with HCC. Note the lower noise and higher CNR on mono+ images, rendering the HCC better visible. B, Axial images at 190 keV with mono (left) and mono+ (right) of a 56-year-old patient and a hypoattenuating HCC. Note the lower noise and better conspicuity of the hypoattenuating lesion on mono+ image. Owing to high keV, the intravenous contrast is not visualized.

© 2015 Wolters Kluwer Health, Inc. All rights reserved.

Copyright © 2015 Wolters Kluwer Health, Inc. Unauthorized reproduction of this article is prohibited.

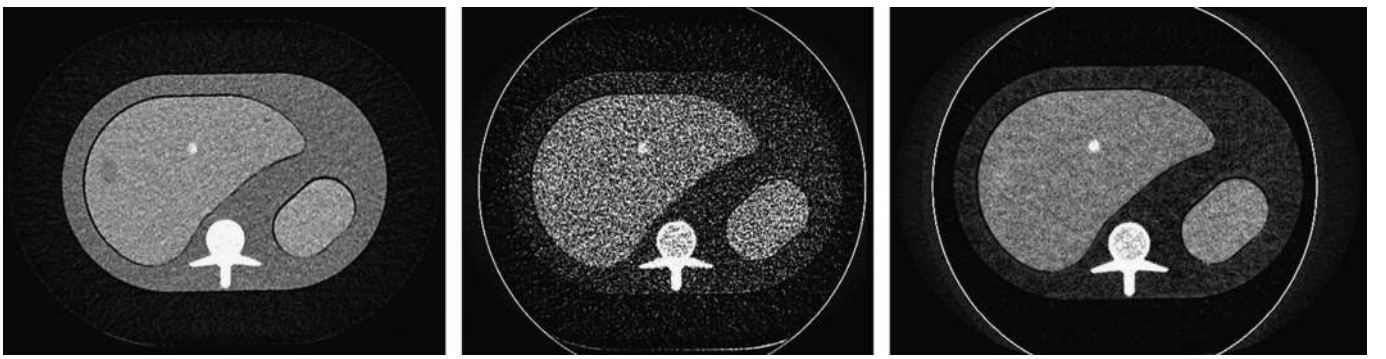

FIGURE 5. Axial images of the large phantom with single energy (120 kV[p], left) and at 40 keV with mono (middle) and mono+ (right). Note the high image noise on mono images, the fair contrast on single-energy images, and the high contrast and low image noise on mono+ images at 40 keV, increasing the conspicuity of the hyperattenuating lesion.

than for mono (detailed results exemplarily for the medium-sized phantom in Table 3).

DISCUSSION

Owing to variable mass attenuation coefficients of different tissue, imaging at different kiloelectron volt levels might be advantageous compared to a fixed tube voltage level for improved lesion detection.[12] The recently introduced advanced monoenergetic image reconstruction algorithm (mono+) mixes images with high contrast (and high noise) with those having low image noise (and medium contrast) to improve the CNR.[12] In this study, we investigated into the value of this algorithm in comparison with the standard monoenergetic algorithm for the visualization of both hyperattenuating and hypoattenuating liver lesions in various body sizes both in phantoms and patients.

At low tube voltages, more low-energy photons are emitted with the polyenergetic x-ray beam and are absorbed by the scanned object resulting in beam-hardening artifacts and scatter noise.[11] Virtual monoenergetic images are reconstructed with improved attenuation linearity and are intended to resemble an acquisition performed with x-rays at a single energy level. However, as being reconstructed from polyenergetic data, monoenergetic data still suffer from scatter noise at low-energy data sets.[11] As expected, we found substantially lower image noise on mono+ images than on mono images in all phantom sizes and patients. This is explained by the mono+ algorithm itself, which combines the high contrast properties of low kiloelectron volt images and the low image noise of high–kiloelectron volt images.

Lesions with iodinated contrast agent uptake yield increased attenuation at decreasing kiloelectron volt levels while approaching the k-edge of iodine at 33 keV. Consequently, arterial-phase 80-kV(p) images have previously been reported to be more sensitive in detecting hypervascular liver lesions than those at 120 kV(p).[16] In this study, the authors used polyenergetic images from dual-energy CT with blending of low- and high-kilovoltage tube image data to approximate a 120-kV(p) single-energy CT data set. In our study, the mono+ algorithm was associated with a steady increase of CNR at decreasing energy levels for hyperattenuating lesions due to the increasing iodine contrast, with the highest CNR at 40 keV in the small to large phantom size. In distinction, the highest CNR in the XL phantom size was found at 80 keV in both mono and mono+, indicating that there is a technical limitation of the advanced monoenergetic algorithm to compensate exceptional high image noise in morbidly obese patients. In patients with hyperattenuating HCC, lesions behaved similarly to those in the phantom; however, the effect was more pronounced because the high attenuation values of the lesion relative to the surrounding liver are mainly derived from iodine and not from soft tissue contrast.

A recent study using polyenergetic images from dual-energy CT showed that portal venous phase 80-kV(p) images are more sensitive in detecting hypovascular liver lesions than on blended low- and high-kilovoltage images (approximating 120-kV[p] images).[17] In our study,

TABLE 2. Average Lesion Conspicuity Scores Among All Kiloelectron Volt Energy Levels for Liver Lesions on Mono and Mono+ Image Data Sets and for Single Energy (120 kV[p])

		Reader 1		Reader 2	
		Hyperattenuating	Hypoattenuating	Hyperattenuating	Hypoattenuating
S	Mono	1.9	2.3	1.9	2.8
	Mono+	2.9	3.5	2.8	3.3
	120 kV(p)	3.5	2.5	4	2.5
M	Mono	2	2.3	2.1	2.3
	Mono+	2.6	3.0	2.7	3.0
	120 kV(p)	3.5	2.5	3.5	3
L	Mono	1.8	1.8	1.8	1.8
	Mono+	2.3	2.1	2.3	2.1
	120 kV(p)	3.5	1.5	3.5	1.5
XL	Mono	1.2	1	1.3	1
	Mono+	1.3	1	1.3	1
	120 kV(p)	2	1	2	1

© 2015 Wolters Kluwer Health, Inc. All rights reserved.

Copyright © 2015 Wolters Kluwer Health, Inc. Unauthorized reproduction of this article is prohibited.

TABLE 3. Lesion Conspicuity Scores in the Medium-Sized Phantom (350 × 250 mm)

	Lesion 1 Hyperattenuating			Lesion 2 Hyperattenuating			Lesion 3 Hypoattenuating			Lesion 4 Hypoattenuating		
keV	**Mono**	**Mono+**	**120 kV(p)**	**Mono**	**Mono+**	**120 kV(p)**	**Mono**	**Mono+**	**120 kV(p)**	**Mono**	**Mono+**	**120 kV(p)**
40	4	**5**		1	**3**		1	1		1	1	
50	**5**	**5**		1	**3**		1	1		1	1	
60	**5**	**5**		1	**3**		2	1.5		1	1.5	
70	**5**	**5**		1.5	**3**		2.5	2		1	2	
80	4.5	**5**		2	**3**		3	2.5		2	2	
90	4	**5**		2.5	**3**		**4**	3.5		2	2	
100	3	4		**3**	2.5		**4**	4		2	2.5	
110	2.5	3.5		2	2		**4**	**5**		2	**3**	
120	2	3	**5**	2	2	**2**	**4**	**5**	**3.5**	**3**	**3**	**2**
130	1.5	2.5		1	2		**4**	**5**		**3**	**3**	
140	1	2		1	1.5		**4**	**5**		2	**3**	
150	1	2		1	1		3.5	**5**		1.5	**3**	
160	1	1.5		1	1		3	4		1	**3**	
170	1	1		1	1		3	4		1	**3**	
180	1	1		1	1		2.5	4		1	**3**	
190	1	1		1	1		2.5	3.5		1	**3**	

Highest scores are set in bold.

we found that the phantom hypoattenuating lesions did indeed demonstrate highest CNR at 80 keV on mono images; however, highest CNR was found on mono+ images at 190 keV. In distinction to patient results in hyperattenuating lesions, we found differences between the phantom and patient results regarding CNR curves for hypoattenuating HCC lesions. Explanations for these finding in patient data need to take into account the nature and content of the hypodense liver lesion. In general, 2 types of hypoattenuating liver lesions can be differentiated. First, cystic lesions contain no iodine, whereas the surrounding liver contains iodine. In this case, higher CNR is found at lower kiloelectron volt owing to higher attenuation of the liver resulting in higher contrast to the cystic lesion. Second, in cases of necrosis with small amounts of iodine CNR can be constant at all kiloelectron volt levels, if the iodine concentration is similar to that in the adjacent liver, with no beneficial effect at low– or high–kiloelectron volt levels.

In our study, mono+ images were found to be superior to the conventional mono algorithm and single-energy images at 120 kV(p) for objective image quality both ex vivo and in vivo, as well as in regard to lesion conspicuity of both hyperattenuating and hypoattenuating liver lesions. In our phantom containing a liver without iodine, the hyperdense iodinated lesions were more conspicuous on low–kiloelectron volt mono+ images owing to the iodine-induced contrast, whereas hypoattenuating (less iodinated) lesions were more conspicuous on high–kiloelectron volt mono+ images. This latter result was found both ex vivo and in-vivo and was reflected in both quantitative and qualitative results on high–kiloelectron volt images for hypoattenuating lesions. With increasing phantom sizes, the conspicuity scores decreased for both hyperattenuating and hypoattenuating lesions. In the largest-size phantom, the hypoattenuating liver lesions could not be detected by both readers, and the CNR of hypoattenuating lesions in the largest phantom was lower on mono+ images than on mono images. This most probably indicates a size limitation for dual-energy CT at the protocol parameters used in this study. This is further substantiated by the fact that in the XL phantom, single-energy CT at 120 kV(p) outperformed both the mono and the mono+ algorithm in regard to the CNR of hyperattenuating and mono+ for hypoattenuating liver lesions owing to higher noise levels. This was, however, not reflected in the lesion conspicuity scores.

In a practical sense, the following approach to liver lesions could be advocated based on the results from this study. When CT data were acquired with dual energy and in the portal-venous phase of enhancement in a patient with a liver lesion, readers should use the mono+ algorithm with manual selection of kiloelectron volt levels for obtaining a better visualization of both hyperattenuating and hypoattenuating lesions. If liver lesions are hyperattenuating, low kiloelectron volt levels (ie, 40 keV) should be selected, and when lesions are hypoattenuating the high–kiloelectron volt images (ie, 190 keV) should be used for further image interpretation. In morbidly obese patients, CT of the liver should be performed with single energy.

We have to acknowledge some study limitations. First, the number of included patients and the number of lesions in these patients were relatively low, and other lesions such as, for example, metastases from different underlying entities should be included in future studies. The advantages of our phantom setting, however, are the exact knowledge of lesion size, density, and location, and the option to investigate the same lesions in various patient sizes. Second, the attenuation of the phantom liver represents that of a homogeneous late arterial phase, not including heterogeneous areas that might be present in patients with chronic liver disease. In addition, the liver insert itself does not contain iodine, similar to the study by Grant et al[12] and as in many other liver phantom studies and therefore does not properly reflect the proper in vivo contrast at all kiloelectron volt levels. However, because of this shortcoming, we included also patient data into this study for simulating a realistic in vivo scenario. Finally, this study only evaluated image quality, and future studies with a sufficiently large number of patients and a suitable reference standard will be needed to show whether the mono+ algorithm actually increases the sensitivity for liver lesion detection. In addition, the issue of specificity must be addressed in these future studies to evaluate whether this algorithm might introduce false-positive findings.

In conclusion, our ex vivo and patient data indicate that advanced virtual monoenergetic CT images result in stable attenuation values, decreased noise, increased CNR, and higher lesion conspicuity of both hyperattenuating and hypoattenuating liver lesions. The algorithm, however, has limitations in morbidly obese body sizes.

© 2015 Wolters Kluwer Health, Inc. All rights reserved.

Copyright © 2015 Wolters Kluwer Health, Inc. Unauthorized reproduction of this article is prohibited.

REFERENCES

1. Marin D, Nelson RC, Samei E, et al. Hypervascular liver tumors: low tube voltage, high tube current multidetector CT during late hepatic arterial phase for detection—initial clinical experience. *Radiology*. 2009;251:771–779.
2. Chang W, Lee JM, Lee K, et al. Assessment of a model-based, iterative reconstruction algorithm (MBIR) regarding image quality and dose reduction in liver computed tomography. *Invest Radiol*. 2013;48:598–606.
3. Park M, Chung YE, Lee HS, et al. Intraindividual comparison of diagnostic performance in patients with hepatic metastasis of full-dose standard and half-dose iterative reconstructions with dual-source abdominal computed tomography. *Invest Radiol*. 2014;49:195–200.
4. Mieville FA, Gudinchet F, Brunelle F, et al. Iterative reconstruction methods in two different MDCT scanners: physical metrics and 4-alternative forced-choice detectability experiments—a phantom approach. *Phys Med*. 2013;29:99–110.
5. Husarik DB, Schindera ST, Morsbach F, et al. Combining automated attenuation-based tube voltage selection and iterative reconstruction: a liver phantom study. *Eur Radiol*. 2014;24:657–667.
6. Yu L, Leng S, McCollough CH. Dual-energy CT-based monochromatic imaging. *AJR Am J Roentgenol*. 2012;199(suppl 5):S9–S15.
7. Meinel FG, Bischoff B, Zhang Q, et al. Metal artifact reduction by dual-energy computed tomography using energetic extrapolation: a systematically optimized protocol. *Invest Radiol*. 2012;47:406–414.
8. Apfaltrer P, Sudarski S, Schneider D, et al. Value of monoenergetic low-kV dual energy CT datasets for improved image quality of CT pulmonary angiography. *Eur J Radiol*. 2014;83:322–328.
9. Schneider D, Apfaltrer P, Sudarski S, et al. Optimization of kiloelectron volt settings in cerebral and cervical dual-energy CT angiography determined with virtual monoenergetic imaging. *Acad Radiol*. 2014;21:431–436.
10. Okayama S, Seno A, Soeda T, et al. Optimization of energy level for coronary angiography with dual-energy and dual-source computed tomography. *Int J Cardiovasc Imaging*. 2012;28:901–909.
11. Sudarski S, Apfaltrer P, Nance JW Jr, et al. Objective and subjective image quality of liver parenchyma and hepatic metastases with virtual monoenergetic dual-source dual-energy CT reconstructions: an analysis in patients with gastrointestinal stromal tumor. *Acad Radiol*. 2014;21:514–522.
12. Grant KL, Flohr TG, Krauss B, et al. Assessment of an advanced image-based technique to calculate virtual monoenergetic computed tomographic images from a dual-energy examination to improve contrast-to-noise ratio in examinations using iodinated contrast media. *Invest Radiol*. 2014;49:586–592.
13. Morsbach F, Desbiolles L, Plass A, et al. Stenosis quantification in coronary CT angiography: impact of an integrated circuit detector with iterative reconstruction. *Invest Radiol*. 2013;48:32–40.
14. Bongartz G, Golding SJ, Jurik AG. European guidelines on quality criteria for computed tomography. *European Commission*. 2000: 16262.
15. Landis JR, Koch GG. The measurement of observer agreement for categorical data. *Biometrics*. 1977;33:159–174.
16. Altenbernd J, Heusner TA, Ringelstein A, et al. Dual-energy-CT of hypervascular liver lesions in patients with HCC: investigation of image quality and sensitivity. *Eur Radiol*. 2011;21:738–743.
17. Robinson E, Babb J, Chandarana H, et al. Dual source dual energy MDCT: comparison of 80 kVp and weighted average 120 kVp data for conspicuity of hypovascular liver metastases. *Invest Radiol*. 2010;45:413–418.

© 2015 Wolters Kluwer Health, Inc. All rights reserved.

Copyright © 2015 Wolters Kluwer Health, Inc. Unauthorized reproduction of this article is prohibited.